

Suitability of body force model for pressure-difference driven flow in porous media

Guang Yang, Moran Wang^{*}

Department of Engineering Mechanics, Tsinghua University, Beijing 100084, China

ARTICLE INFO

Keywords:

Porous media
LBM
Pore-scale simulation
Multiphase flow
Body force model

ABSTRACT

Pore-scale direct numerical simulation is an important tool for studying the flow of porous media nowadays. This work validates the suitability of body force model for simulating pressure-difference-driven porous flows in pore-scale simulations. The multi-relaxation time lattice Boltzmann method (MRT-LBM) with the color-gradient continuum-surface-force (CG-CSF) model is employed to calculate the absolute and relative permeability of randomly generated porous media. Results show that for single-phase flows, the relative errors are below 5% for most homogeneous porous structures while as high as 80% for structures with preferential paths. This study also reveals the pore-scale flow mechanisms and proposes a new heterogeneity parameter quantified by the standard deviation of the pressure at the boundary. For multiphase flows, errors of the body force model are significant at low Ca due to irreversible phase distribution difference appearing at the early stages. The findings of this work could be applied to other transport processes in porous media. It is crucial to consider the structural heterogeneity and proper parameters when employing the body force model in pore-scale simulations.

1. Introduction

Flow in porous media has attracted significant attention due to its broad applications in energy and environmental fields, such as enhanced oil recovery [1], contaminant transport [2], fuel cells [3] and carbon capture and storage [4]. Recently advancements in imaging technologies and high-performance computing (HPC) have made pore-scale direct numerical simulation (DNS) a powerful tool for studying porous flows [5–7]. Pore-scale DNSs conducted on real pore structures, which can be obtained from X-ray tomographic imaging, are accurate and intuitive, as the flow fields like velocity and phase distribution can be easily visualized in detail [8,9]. Furthermore, pore-scale simulations serve as an important upscaling method for non-Darcy flows [10,11].

Among the various pore-scale DNS methods available, the lattice Boltzmann method (LBM) is one of the most popular methods due to its ability to handle complex boundaries and complex fluids in porous media and its utilization of modern computing architectures in HPC, such as GPUs and coprocessors [5,9,12,13]. As a matter of fact, one of the earliest applications of LBM was predicting the permeability and the relative permeability of sandstones [14–16]. However, similar to any other simulations, obtaining meaningful simulation results is highly dependent on proper boundary conditions.

For single-phase flows, many researchers have proposed pressure boundaries including the non-equilibrium bounce back scheme (sometimes also referred as Zou-He scheme) [17], the non-equilibrium extrapolation scheme [18] and the anti-bounce-back scheme [19]. Assuming periodic flows, Zhang and Kwok [20], and Kim and Pitsch [21] also proposed periodic pressure boundary conditions. Although these boundaries work well for single-phase flows, the pressure boundary conditions for multiphase flows remains a challenge. Wang et al. [76] proposed a periodic boundary condition by extending the Zhang-Kwok scheme to the pseudo-potential LBM [22]. Huang et al. [23] extended Zou-He to the color-gradient LBM for multiphase flows. However, their boundary shows unphysical behavior when both phases exist at the boundaries [23,24]. Leclaire et al. [24] introduced a proportional-integral-derivative (PID) controller to enhance mass conservation in the multiphase periodic pressure boundary [76]. However, this boundary condition is complicated and the pressure difference is achieved via the PID controller which is inactive when both phases appear at the boundaries. Thus, this boundary is not suitable for cases where the gas/liquid-liquid interfaces frequently intersect with the boundaries. More recently, Wang et al. [25] combined Zou-He boundary with outlet convective boundary condition [26] which is limited to outlet boundaries.

^{*} Corresponding author.

E-mail address: mrwang@tsinghua.edu.cn (M. Wang).

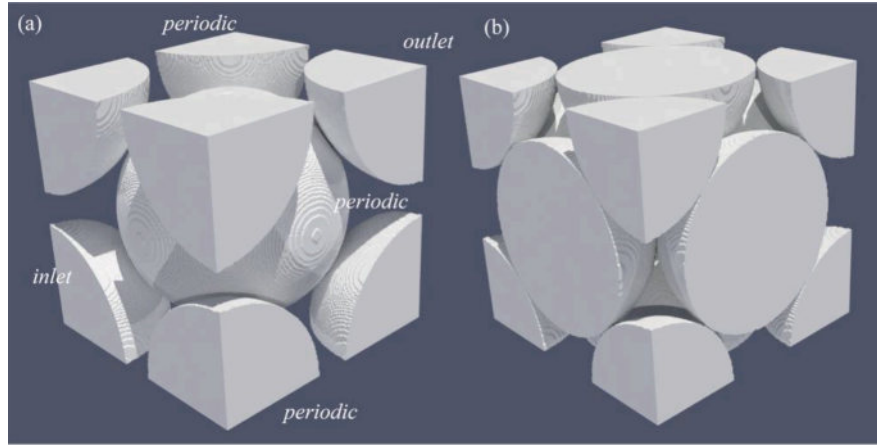


Fig. 1. Structure of body-centered cubic (a, BCC) and face-centered cubic (b, FCC) packs. The pressure boundary is applied at the inlet and outlet while the periodic boundary is employed for other boundaries as the Fig (a) shows.

Table 1

Comparison between the simulated permeability and theoretical permeability on BCC and FCC packs. The results of the permeability are non-dimensionalized by the square of the sphere diameter D .

Structure	Mesh size: L	Sim. $\frac{k}{D^2} \times 10^4$	Ref. $\frac{k}{D^2} \times 10^4$ [71]	Error (%)
BCC	50	4.941	5.023	1.6
$L = 2\sqrt{3}$	100	4.982		0.8
$/\sqrt{3}D$	200	5.040		0.3
	400	5.040		0.3
FCC	50	1.694	1.736	2.4
$L = \sqrt{2}D$	100	1.783		2.7
	200	1.723		0.7
	400	1.723		0.7

Due to the limitations of the pressure boundaries mentioned above, the utilization of body force to simulate pressure-driven flows is commonly adopted in pore-scale DNSs. Generally, an equivalent body force is applied at the simulation domain with the periodic boundary at the main flow direction to replace pressure boundaries [27]. Employment of such approach can be found in various fields, such as single-phase flows [28–31], multiphase flows [27–29,32–41], electrokinetic flows [42–44] and reactive transports [30,38]. These simulations are conducted on various porous structures, including regular channel networks [33], regular sphere packs [40,42,43], random sphere packs [27,36,41,44], fibrous porous media [34] and natural porous media such as sandstones [28–30,32,35,37,38,45] and carbonates [38]. The body force approach is simple, usually more numerically stable and induces fewer boundary effects compared with pressure boundaries [23, 24,26]. However, it is important to recognize that in the lab-experiments and the real world, these flows are driven by pressure gradient. Therefore, it is critical to determine whether the body force approach can accurately simulate pressure boundaries for porous flows.

The aforementioned problem was first investigated by Kandhai et al. [46] who simulated the flow over a cylinder and found that the error was smaller than 5% for the Reynolds number Re they considered. Other researchers have also explored the difference between the pressure boundary and the body force approach over simple geometries, yielding similar results [20,21]. For porous flows, such small differences can be safely neglected. Rustamov et al. [47] studied the difference in mass conservation and convergence behavior between pressure boundary, body force and periodic pressure boundary on rarified gas flow in porous media. Zakirov and Khamchenkov [31] examined the boundary effects on the prediction of the permeability tensor of heterogeneous porous media. They reported the differences can be neglected for diagonal

components of the permeability tensor. However, their work is statistical and engineering-oriented. The results are averaged over different structures with the same heterogeneity. Thus, previous investigations mainly focused on simple geometries and single-phase flows. The structural heterogeneity effect and multiphase effect, especially the underlying flow mechanisms remain largely unexplored.

In this work, we focus on the absolute permeability and the relative permeability calculations as two classical examples to validate the suitability of replacing the pressure boundary approach with the body force model. LBM with multiple-relaxation-time (MRT) model and the color-gradient continuum-surface-force (CG-CSF) scheme is employed to simulate single-phase and multiphase flows. Additionally, a new heterogeneity parameter is proposed to quantitatively describe the suitability of the body force approach for single-phase flows. For multiphase flows, we discuss the effect of gas/liquid-liquid interfaces via the capillary number Ca . Subsequent to the introduction, we outline the reminder of this work as follows. In Section 2, a brief introduction on single-phase LBM, multiphase LBM algorithms and corresponding boundary conditions will be provided. Then we conduct several benchmarks to validate our models in Section 3. In Section 4, we study the structural heterogeneity and multiphase effects on body force approach and pressure boundary approach. Our conclusions will be presented in Section 5.

2. Model and method

2.1. Single-phase LBM

Derived from the kinetic theory, the fluid transport in LBM is represented by a set of particles moving on lattices [48]. Generally, the lattice Boltzmann equation with a Bhatnagar-Gross-Krook (BGK, also known as single-relaxation time model or SRT) collision term and force term can be expressed as [49]

$$f_i(x + c_i \delta t, t + \delta t) = f_i(x, t) + \Omega_i + \bar{F}_i, \quad (1)$$

with

$$\Omega_i = -\frac{\delta t}{\tau} (f_i - f_i^{eq}), \quad (2)$$

$$f_i^{eq} = \rho \omega_i \left[1 + 3 \frac{c_i \cdot u}{c^2} + \frac{9}{2} \frac{(c_i \cdot u)^2}{c^4} - \frac{3}{2} \frac{u \cdot u}{c^2} \right], \quad (3)$$

$$\bar{F}_i = \left(1 - \frac{\delta t}{2\tau} \right) \omega_i \left[3 \frac{c_i \cdot u}{c^2} + 9 \frac{(c_i \cdot u)}{c^4} \right] \cdot F, \quad (4)$$

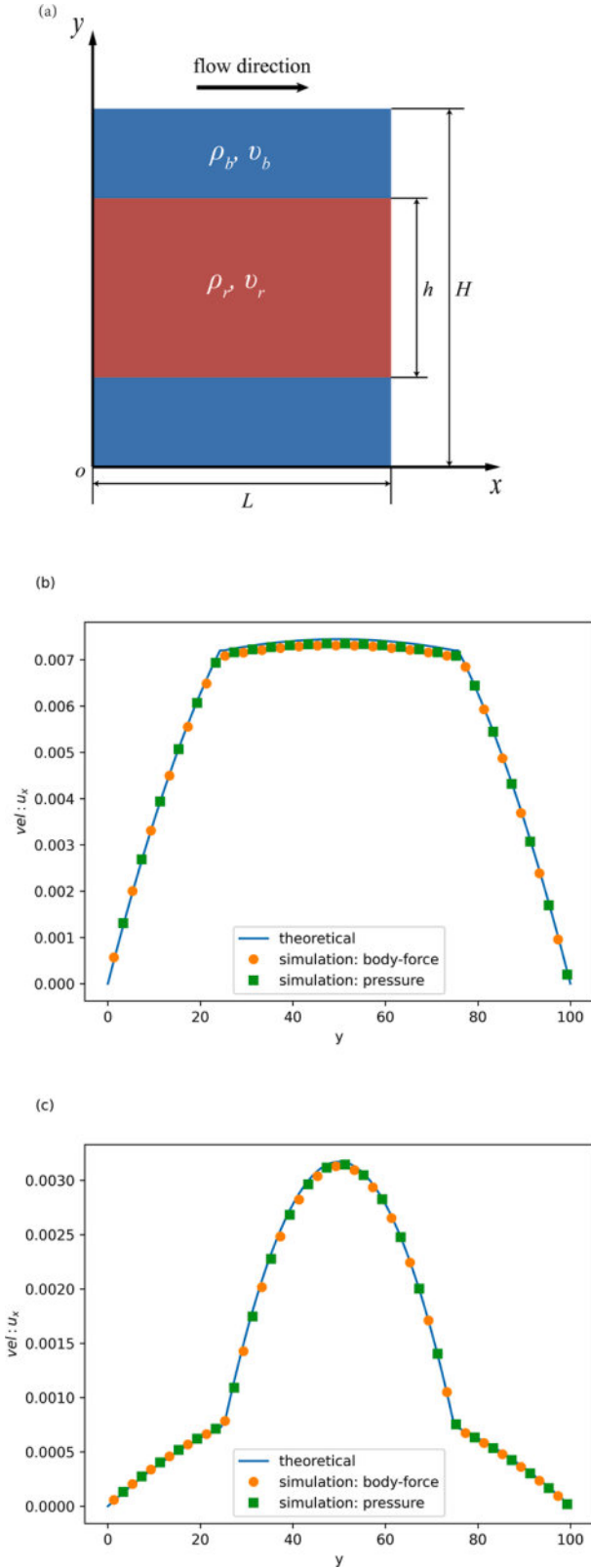


Fig. 2. (a) Schematic of the two-phase layered flow. The non-wetting phase (denoted by red) flows between the wetting phase (denoted by blue). (b, c) Simulated velocity profile along y axis of the body force (orange circle) and pressure boundary (green square) compared with the analytical solutions (line). (a) viscosity ratio $M = 10$; (b) viscosity ratio $M = 0.1$.

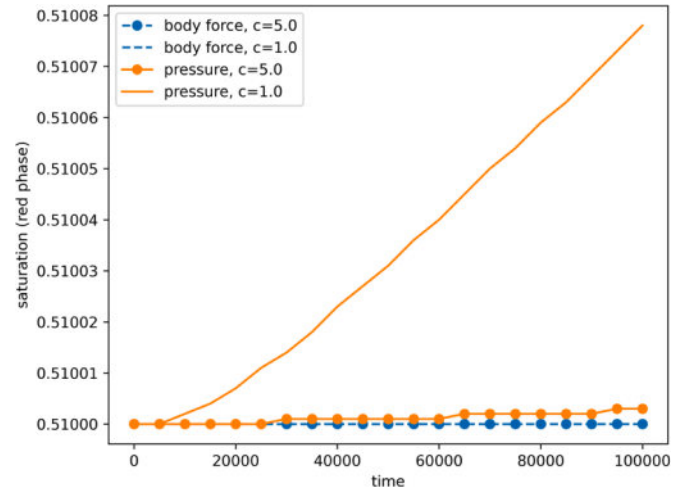


Fig. 3. Simulated saturation of the red (non-wetting) phase over time. The color denotes the lattice speed: orange for $c = 5.0$ and blue for $c = 1.0$, while the line style denotes the boundary condition, solid line for the pressure boundary and dashed line for the body force with periodic boundary.

where $f_i(x, t)$ denotes the (particle) distribution function moving along the velocity c_i at the lattice site x and time step t ; τ is the relaxation time, $f_i^{eq}(x, t)$ is the equilibrium distribution function and \bar{F}_i is the source term related to the external body force F via Eq. (4) [50]. δx and δt denotes the spatial and temporal discretization. The macroscopic variables fluid density ρ and velocity u can be derived via

$$\rho = \sum_i f_i, \quad \rho u = \sum_i f_i c_i + \frac{\rho F \delta t}{2}, \quad (5)$$

Through the Chapman-Enskog expansion, the classical Navier-Stokes equation can be obtained in the low Ma (Mach number, $Ma = \sqrt{3}u/c$) region, where $c = \delta x/\delta t$ is the lattice speed. For D3Q19 lattice we employed in this work, the fluid pressure p and the viscosity ν in N-S equation are given

$$p = \frac{1}{3}\rho c^2, \quad \nu = \frac{1}{3}c^2 \left(\tau - \frac{\delta t}{2} \right). \quad (6)$$

For two-dimensional simulations, the periodic boundary condition is applied at the z -direction.

To achieve better accuracy and stability, the multiple-relaxation time (MRT) [51–53] framework is employed, in which the collision step is conducted in the moment space, i.e.

$$f_i(x + c_i \delta t, t + \delta t) = f_i(x, t) - M^{-1} S (M f(x, t) - m^{eq}) + \delta t M^{-1} \left(I - \frac{S}{2} \right) \hat{F}, \quad (7)$$

where f and $m^{eq} = M f^{eq}$ represent the vector form of the distribution functions and equilibrium moments, respectively; M denotes the transformation matrix to the moment space and $\hat{F} = M \bar{F}$ denotes the external force term in the moment space [54,55]. Though the equilibrium moments m^{eq} and the force moments \hat{F} can be derived using the transformation matrix, for the purpose of high computing efficiency, the aforementioned moments are calculated directly from the macroscopic variables following [49,56],

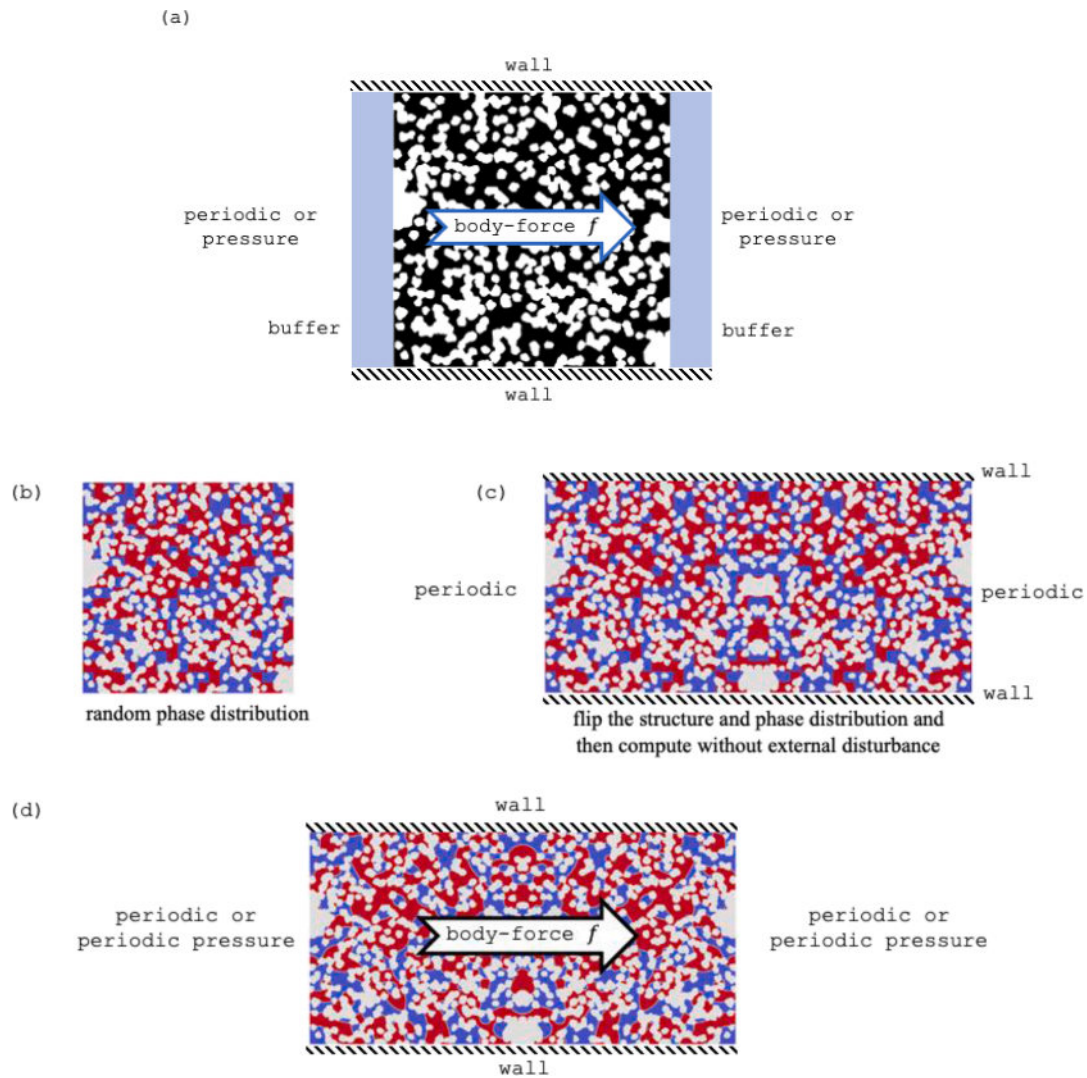


Fig. 4. (a) Numerical setup of the permeability calculation. The buffer width is 10 lattices unless otherwise specified. (b, c, d) Numerical setup of the relative permeability calculation. (b) A block-wise random phase distribution with a predetermined saturation is generated in the pore space. (c) Both the structure and phase distribution are flipped. Then the multiphase LBM is conducted with the periodic boundary at inlet and outlet while no-slip wall applied to other boundaries to achieve local thermal equilibrium. No external driven force is applied in this process. (d) The phase distribution obtained in the previous step is used as the initial condition to calculate the relative permeability under both boundary conditions.

Table 2

Simulated permeability of the homogenous structures. k_{pr} represents the permeability predicted via pressure approach while k_{bf} represents the permeability predicted via body force approach. Err represents the relative error which is defined as $(k_{bf} - k_{pr})/k_{pr}$ (hereafter).

No.	k_{pr}	k_{bf}	Err (%)
1	6.09	5.9	-3.19
2	5.99	5.83	-2.76
3	6.09	5.88	-3.38
4	6.61	6.4	-3.13
5	5.37	5.19	-3.24
6	5.12	5.04	-1.61
7	5.49	5.43	-1.07
8	4.48	4.21	-6.01
9	6.43	6.25	-2.78
10	6.46	6.10	-5.54

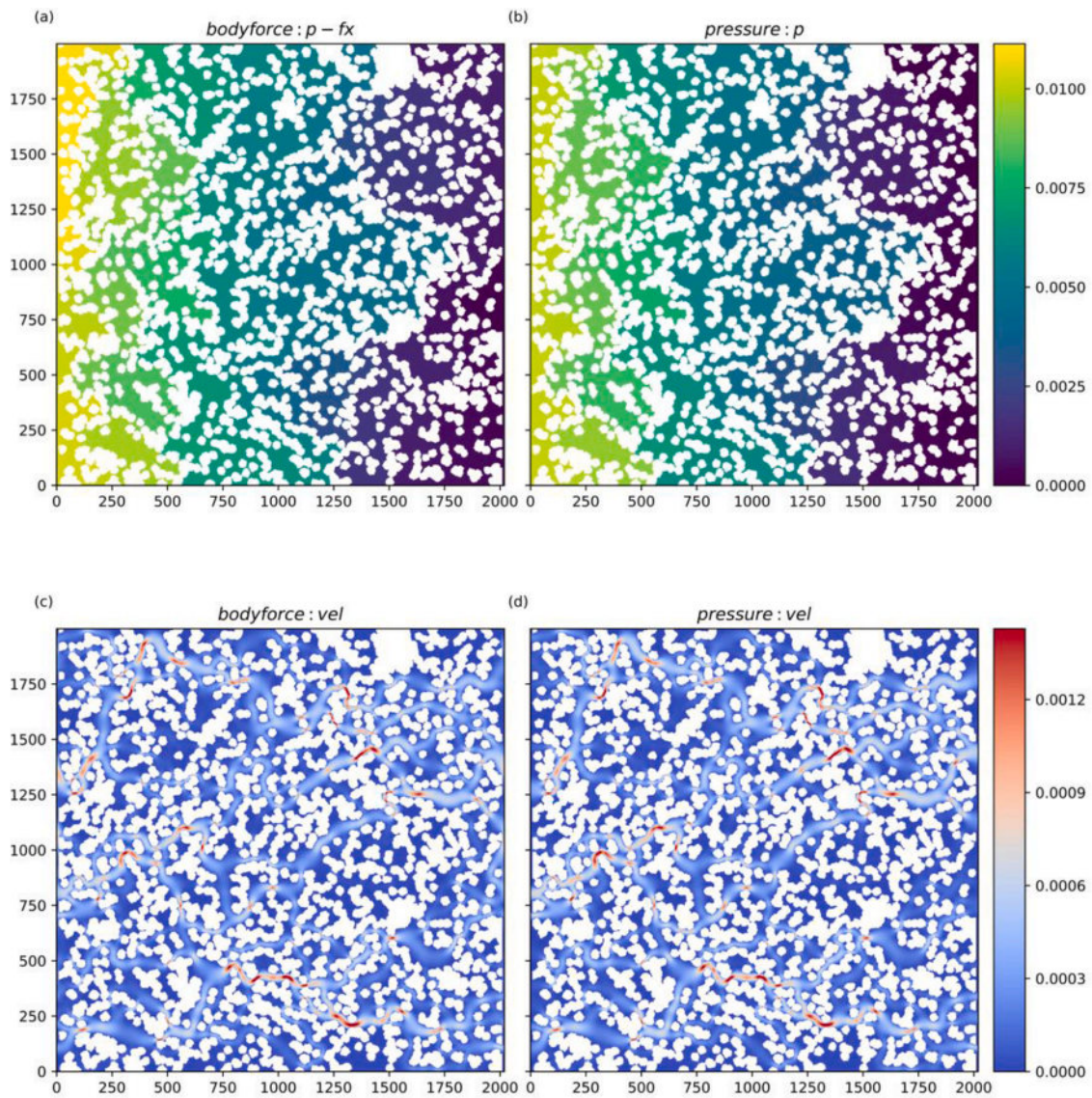


Fig. 5. The simulated pressure field (a, b) and velocity field (c, d) of structure No.9 via body force approach (a, c) and pressure approach (b, d). $Re \approx 0.001$. In the body force approach, the effective pressure field is presented.

Table 3
Simulated permeability of the homogenous structures.

No.	$Re \sim 0.001$			$Re \sim 0.1$			$Re \sim 10$		
	k_{pr}	k_{bf}	Err(%)	k_{pr}	k_{bf}	Err(%)	k_{pr}	k_{bf}	Err(%)
1	6.09	5.90	-3.19	5.96	5.77	-3.11	2.37	2.29	-3.10
2	5.99	5.83	-2.76	5.85	5.69	-2.72	2.41	2.39	-0.93
3	6.09	5.88	-3.38	5.96	5.76	-3.32	2.44	2.42	-0.82
4	6.61	6.40	-3.13	6.47	6.27	-3.12	2.77	2.75	-0.86
5	5.37	5.19	-3.24	5.27	5.10	-3.28	2.37	2.31	-2.31

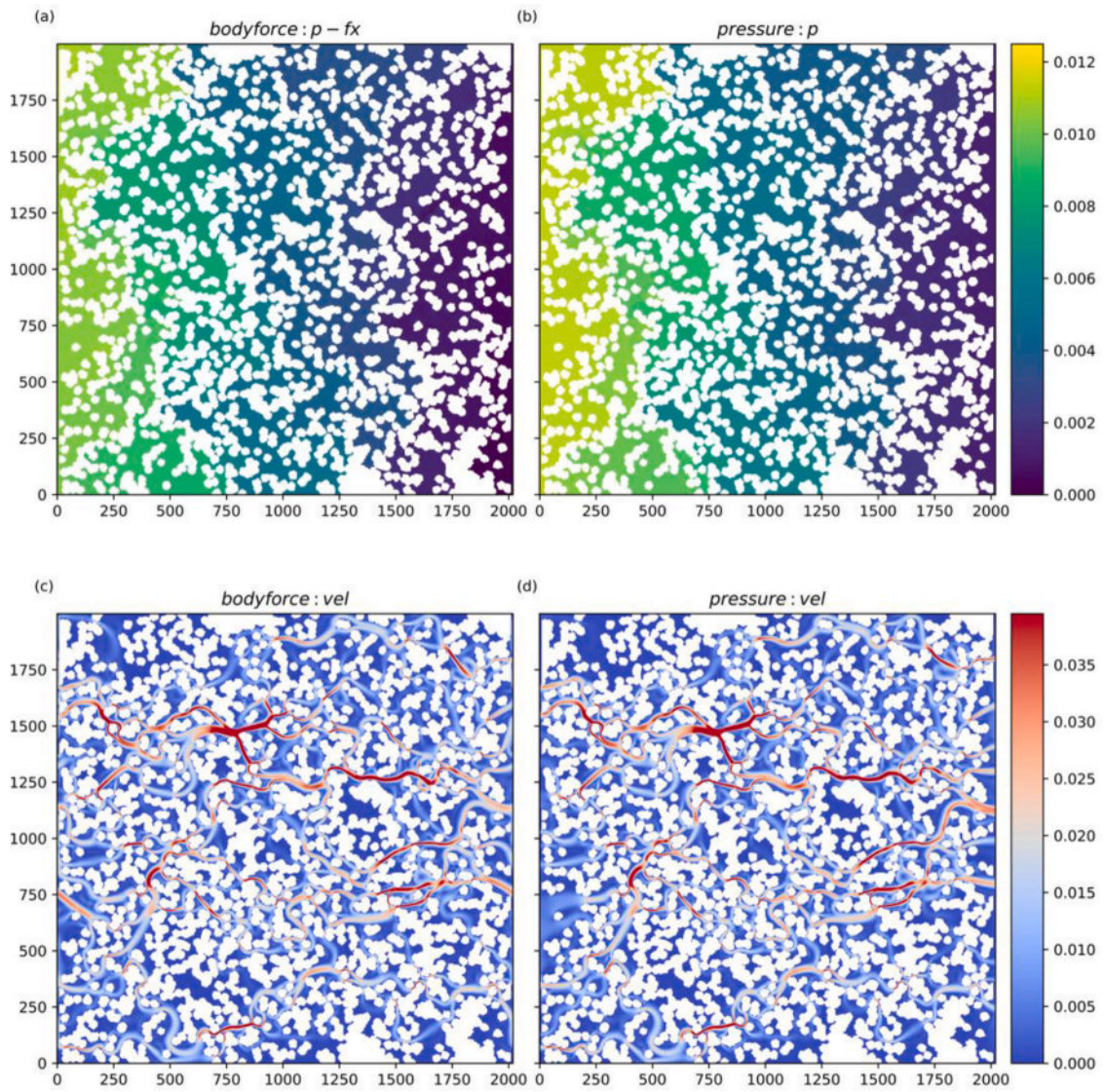


Fig. 6. The simulated pressure field (a, b) and velocity field (c, d) of structure No.2 via the body force approach (a, c) and pressure approach (b, d). $Re \approx 10$. In the body force approach, the effective pressure field is present d.

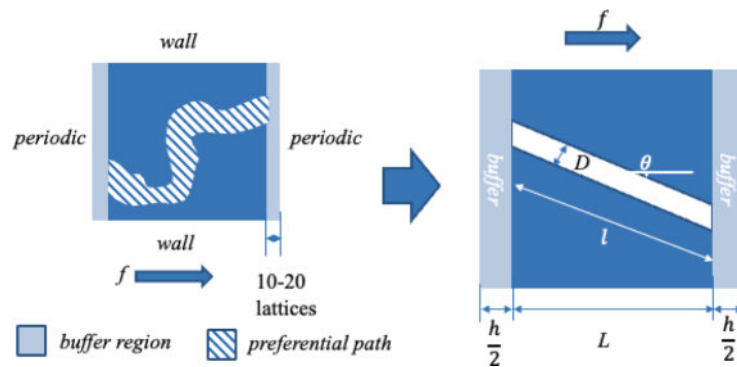


Fig. 7. Illustration of the simplified model of the porous media with preferential path.

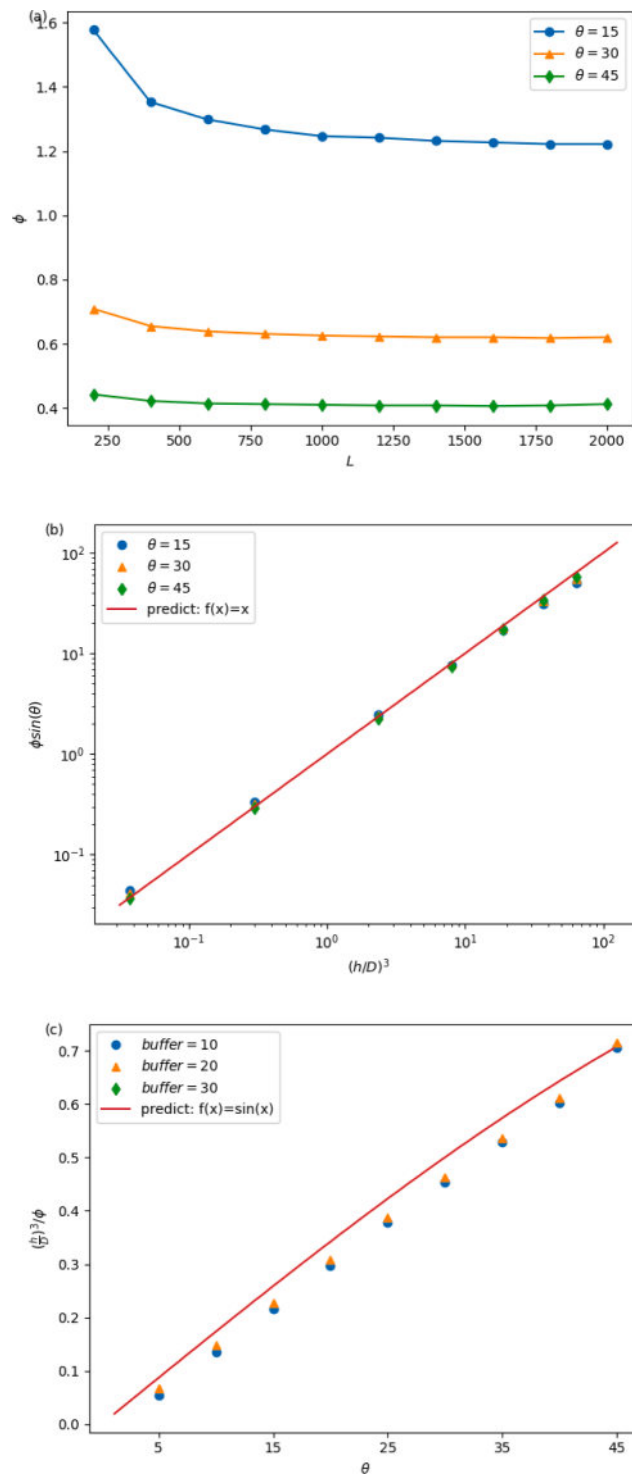


Fig. 8. Comparisons of the simulated results and Eq. (30). (a) Simulated results of ϕ as the function of porous media length. (b) Simulated results of $\phi \sin(\theta)$ as the function of $(\frac{h}{D})^3$ compared with the theoretical prediction. (c) Simulated results of $(\frac{h}{D})^3 / \phi$ as the function of θ compared with the theoretical prediction.

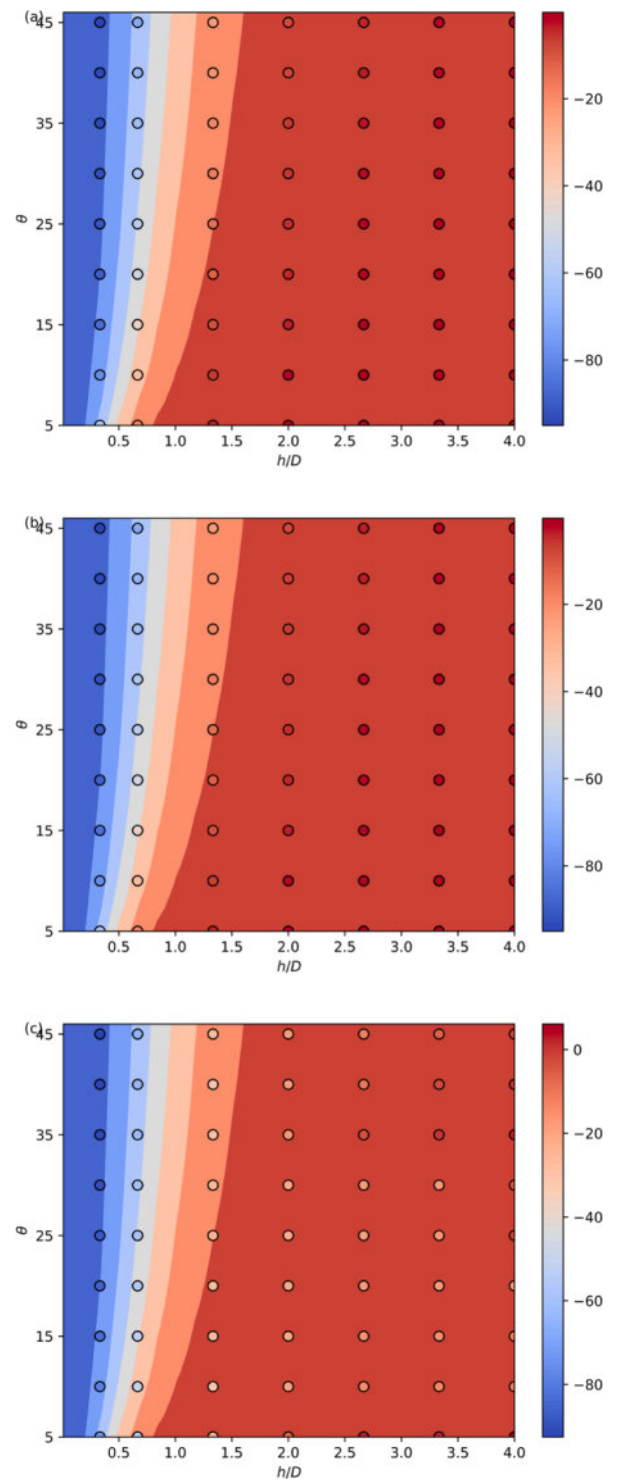


Fig. 9. Comparisons of the simulated results and theoretical model at different Re . Dots are simulated results and the contour is predicted via Eq. (29,30). (a) $Re = 0.002$. (b) $Re = 0.2$. (c) $Re = 12$.

$$\mathbf{m}^{eq} = \begin{bmatrix} \rho \\ -11\rho + 19\rho(u_x^2 + u_y^2 + u_z^2) \\ 3\rho - \frac{11}{2}\rho(u_x^2 + u_y^2 + u_z^2) \\ \rho u_x \\ \frac{2}{3}\rho u_x \\ \rho u_y \\ \frac{2}{3}\rho u_y \\ \rho u_z \\ \frac{2}{3}\rho u_z \\ \rho(2u_x^2 - u_y^2 - u_z^2) \\ -\frac{1}{2}\rho(2u_x^2 - u_y^2 - u_z^2) \\ \rho(u_y^2 - u_z^2) \\ -\frac{1}{2}\rho(u_y^2 - u_z^2) \\ \rho u_x u_y \\ \rho u_x u_z \\ \rho u_y u_z \\ 0 \\ 0 \\ 0 \\ 0 \end{bmatrix}, \quad \widehat{\mathbf{F}} = \begin{bmatrix} 0 \\ 38\mathbf{u}\cdot\mathbf{F} \\ -11\mathbf{u}\cdot\mathbf{F} \\ F_x \\ \frac{2}{3}F_x \\ F_y \\ \frac{2}{3}F_y \\ F_z \\ \frac{2}{3}F_z \\ 2(2F_x u_x - F_y u_y - F_z u_z) \\ -(2F_x u_x - F_y u_y - F_z u_z) \\ 2(F_y u_y - F_z u_z) \\ -(F_y u_y - F_z u_z) \\ F_x u_x + F_y u_y \\ F_y u_y + F_z u_z \\ F_x u_x + F_z u_z \\ 0 \\ 0 \\ 0 \end{bmatrix}, \quad (8)$$

and \mathbf{S} is a diagonal matrix composed of the relaxation parameters,

$$\mathbf{S} = \text{diag}(S_\rho, S_e, S_\varepsilon, S_j, S_q, S_j, S_q, S_j, S_q, S_\nu, S_\pi, S_\nu, S_\pi, S_\nu, S_\nu, S_m, S_m, S_m), \quad (9)$$

in which S_ν is related to the viscosity via $\frac{1}{S_\nu} = \tau = \frac{3\nu}{c^2 \delta t} + \frac{1}{2}$, while $S_\rho = S_j = 0$ correspond to the conserved moments of density and momentum [52]. For the no-slip bounce-back boundary condition, $S_m = S_q = \frac{8(2-S_\nu)}{8-S_\nu}$ is suggested in [19,57]. Other parameters are adjusted to increase numerical stability according to [52]. Concludingly, in this paper, we select

$$\begin{aligned} S_\rho &= S_j = 0, \\ S_e &= 1.19, \quad S_\pi = S_\varepsilon = 1.4, \\ \frac{1}{S_\nu} &= \tau = \frac{3\nu}{c^2 \delta t} + \frac{1}{2}, \quad S_m = S_q = \frac{8(2-S_\nu)}{8-S_\nu}. \end{aligned} \quad (10)$$

As for boundary conditions, in this work, either the periodic boundary condition with a constant body force or the pressure boundary condition is applied at the inlet and the outlet. For single-phase flow, we adopt the non-equilibrium extrapolation scheme [18] for the pressure boundary condition due to its ease of implementation in 3D. In this scheme, the non-equilibrium parts of the distribution functions at the boundaries are extrapolated from the internal fluid regions, i.e.

$$f_i(x_b, t) = f_i^{eq}(\rho_b, \mathbf{u}_f) + f_i(x_f, t) - f_i^{eq}(\rho_f, \mathbf{u}_f), \quad (11)$$

where the subscript b denotes the boundary node, and f denotes the internal fluid node next to the boundary node along the boundary normal vector. $\rho_b = 3p_b/c^2$ is determined by the given boundary pressure. The no-slip boundary at solid wall is achieved via the standard full-way bounce back.

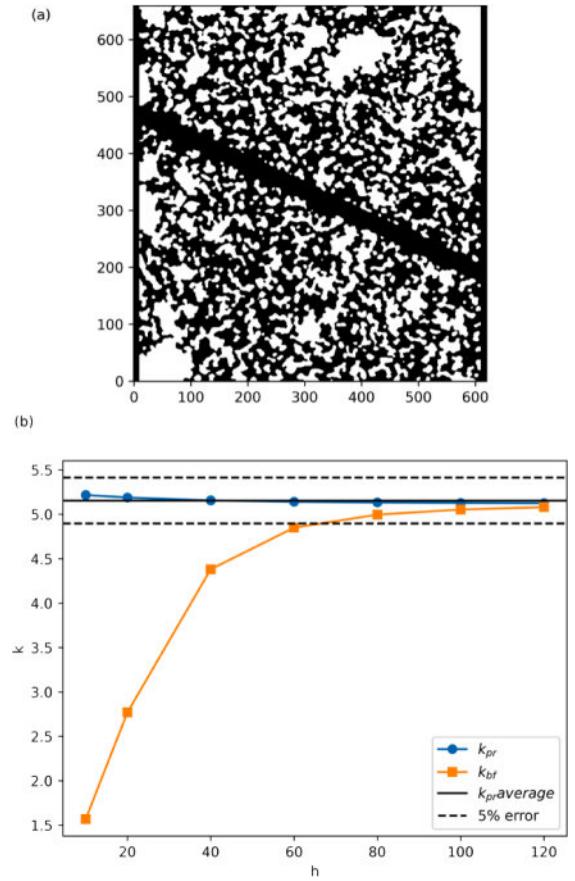


Fig. 10. (a) Illustration of the fracture-matrix porous media. (b) Simulated permeability via the pressure approach and body force approach as the function of buffer size h .

2.2. Multiphase LBM

For the multiphase flow simulation, we adopt the color-gradient (CG) LBM [58–60] with continuum-surface-force (CSF) scheme [61,62]. One of its key features is the ability of adjusting surface tension, fluid viscosity and interface thickness independently [63,64], making it a powerful and versatile tool in simulation of immiscible multiphase flows in porous media. In the CG-CSF model, two sets of the colored distributions, denoted by f_i^b and f_i^r (with b representing blue and r representing red), are adopted to represent the two immiscible fluids. With the MRT framework mentioned above, the transportation of the both fluids can be described by a unique lattice Boltzmann equation:

$$f_i^k(x + \mathbf{e}_i \delta t, t + \delta t) = f_i^k(x, t) + \Omega_i^{2,k} \left[-M^{-1} \mathbf{S} (Mf(x, t) - \mathbf{m}^{eq}) + \delta t M^{-1} \left(\mathbf{I} - \frac{\mathbf{S}}{2} \right) \widehat{\mathbf{F}} \right], \quad (12)$$

Unlike the single-phase LBM, the colored distribution functions are streamed separately while the viscous collision operator is calculated collectively in CG-CSF model [62]. Additionally, the recoloring operator $\Omega_i^{2,k}$ is introduced to minimize the mixing between the two fluids. In this work, the recolor scheme in [63] is applied to the post-collision distribution functions f_i^+ , i.e.,

$$f_i^{+,k}(x, t) = \frac{\rho^k}{\rho^+} f_i^+ \pm \beta \frac{\rho_b \rho_r}{\rho^2} \cos(\psi_i) f_i^{eq}(\rho^k, 0), \quad (13)$$

where

$$\cos(\psi_i) = \frac{|\mathbf{e}_i \cdot \mathbf{C}|}{|\mathbf{e}_i| |\mathbf{C}|}, \quad (14)$$

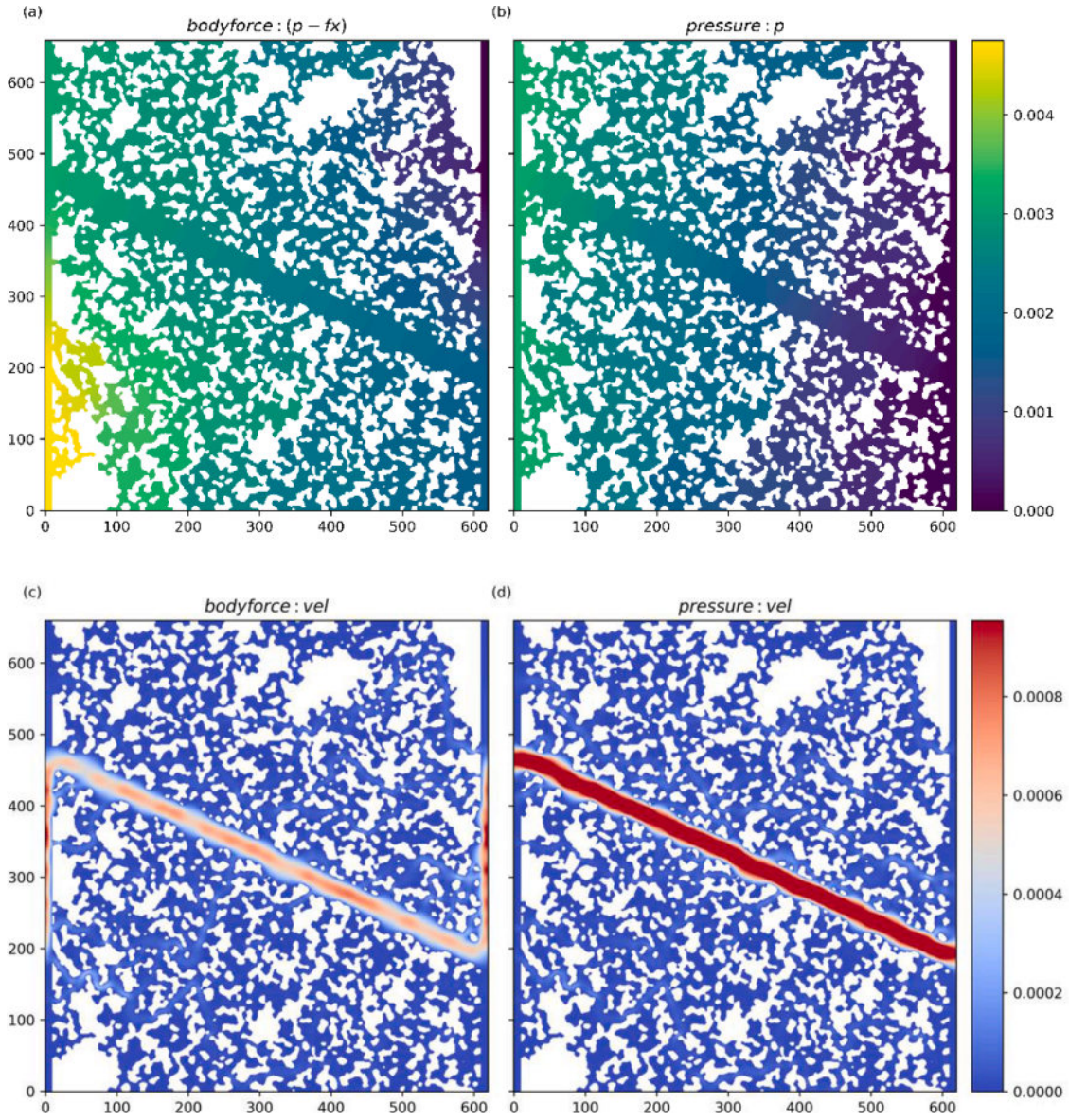


Fig. 11. The simulated pressure field (a, b) and velocity field (c, d) of fracture-matrix structure via body force approach (a, c) and pressure approach (b, d). In the body force approach, the effective pressure field is presented.

f_i^{++k} denotes the colored distribution function after the recolor step. The recolor parameter β is the parameter controlling the interfacial thickness, which ranges from 0 to 1. The interface becomes thinner and numerically instable as β approaches 1. We set β to 0.98 to ensure a sharp interface and good numerical stability.

The interfacial tension is achieved via the body force which is written as [61,62]

$$F = \frac{1}{2} \sigma \kappa C = \frac{1}{2} \sigma \kappa \nabla \phi, \quad (15)$$

where σ and κ represent the interfacial tension and the interfacial curvature; the color gradient, denoted by C can be calculated via the isotropic gradient operator in [65]. Additionally, $\phi = (\rho_r - \rho_b) / (\rho_r + \rho_b)$ is the order parameter, where $\phi = 1$ and $\phi = -1$ indicate the pure fluid r and pure fluid b region, respectively. The interfacial curvature κ can be obtained via the normal direction of the color gradient C (denoted by n) [62], i.e.

$$\kappa = [(I - nn) \cdot \nabla] \cdot n, \quad (16)$$

$$n = \frac{\nabla \phi}{|\nabla \phi|}. \quad (17)$$

Similar to the single-phase LBM, the macroscopic variables are obtained via:

$$\rho^k = \sum_i f_i^k \rho^k u^k = \sum_i f_i^k e_i + \frac{\rho^k F \delta t}{2}, \quad (18)$$

$$\rho = \sum_k \rho^k, \quad \rho u = \sum_k \rho^k u^k, \quad (19)$$

$$p = \frac{1}{3} \rho c^2, \quad \nu_{\text{eff}} = \frac{1}{3} c^2 \left(\tau_{\text{eff}} - \frac{\delta t}{2} \right), \quad (20)$$

where τ_{eff} is the effective relaxation time obtained via the interpolation function [66] to ensure a smooth variation of the relaxation time τ at the interfacial region ($|\phi| < 1$).

To achieve the desired wettability, the geometrical wetting model introduced in [67] is implemented. Firstly suggested by Xu et al. [62], the geometrical wetting model directly modifies the interfacial normal

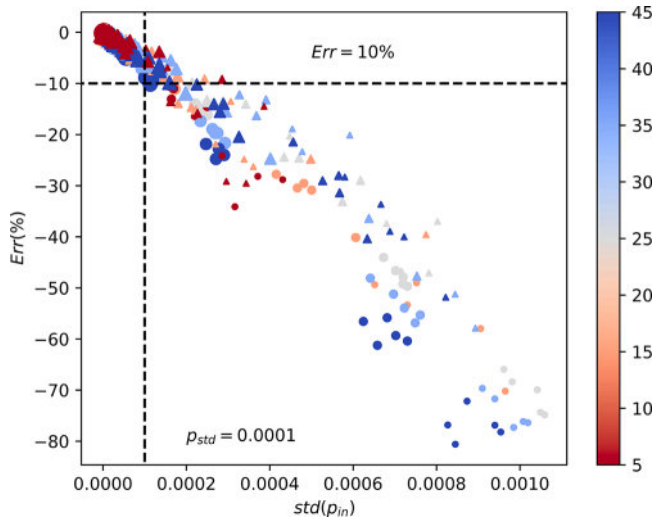


Fig. 12. The relative error as the function of the pressure standard deviation p_{std} at the inlet. The color represents different inclined angles while the marker size denotes buffer size. The marker shape denotes different mean matrix pore sizes. The mean matrix pore size is 8 and 20 respectively for circle markers and triangle markers.

vectors n at the fluid boundary nodes, compared to the fictitious-density model which modifies the fictitious density on the solid boundary nodes. This approach not only removes the unphysical mass transport but also reduces the spurious velocities at boundaries. The desired interfacial normal vector n can be obtained by,

$$n_{\pm} = \left(\cos \pm \theta - \frac{\sin \pm \theta \cos \theta'}{\sin \theta'} \right) n_s + \frac{\sin \pm \theta}{\sin \theta'} n^*, \quad (21)$$

$$\theta' = \arccos(n_s \cdot n^*),$$

where θ , n_s and n^* represent the contact angle, the unit normal vector of the solid and the estimated interfacial direction that obtained from Eq. (17). Then, the interfacial normal vector n is selected based on which one of n_{\pm} has a shorter Euclidean distance to n^* . For complex geometry such as porous media, n_s is calculated by a high-order discretization operator after smoothing the solid structures [62,68]. Additionally, the extrapolation of the order parameter ϕ and the extrapolation of the interface normal vector n are applied to minimize the spurious current at the three-phase contact line region [5,69].

Regarding the inlet and outlet boundaries, the periodic pressure boundary is employed. While ordinary pressure boundary conditions can be applied at inlet and outlet for single-phase flow, they may induce significant boundary effects on the interfacial dynamics and numerical stability [23,24], particularly when both phases appear at boundaries. Therefore, we employ the periodic pressure boundary condition, which ensures a constant saturation for the relative permeability calculation and reduces the aforementioned boundary effects. In this work, we extend the periodic pressure boundary (also known as general periodic boundary) proposed by Kim and Pitsch [21] to multiphase flows.

Consider the post-recolor colored distribution functions f_i^{++k} and the corresponding total distribution function f_i^{++} , which can be decomposed into two parts, i.e., the equilibrium part f_i^{eq} and the non-equilibrium part f_i^{neq} . In Kim and Pitsch [70], the non-equilibrium part of the inlet boundary is approximate with the outlet non-equilibrium distribution function while the equilibrium part is calculated via the local pressure (density) at the inlet and velocity at the outlet, i.e.,

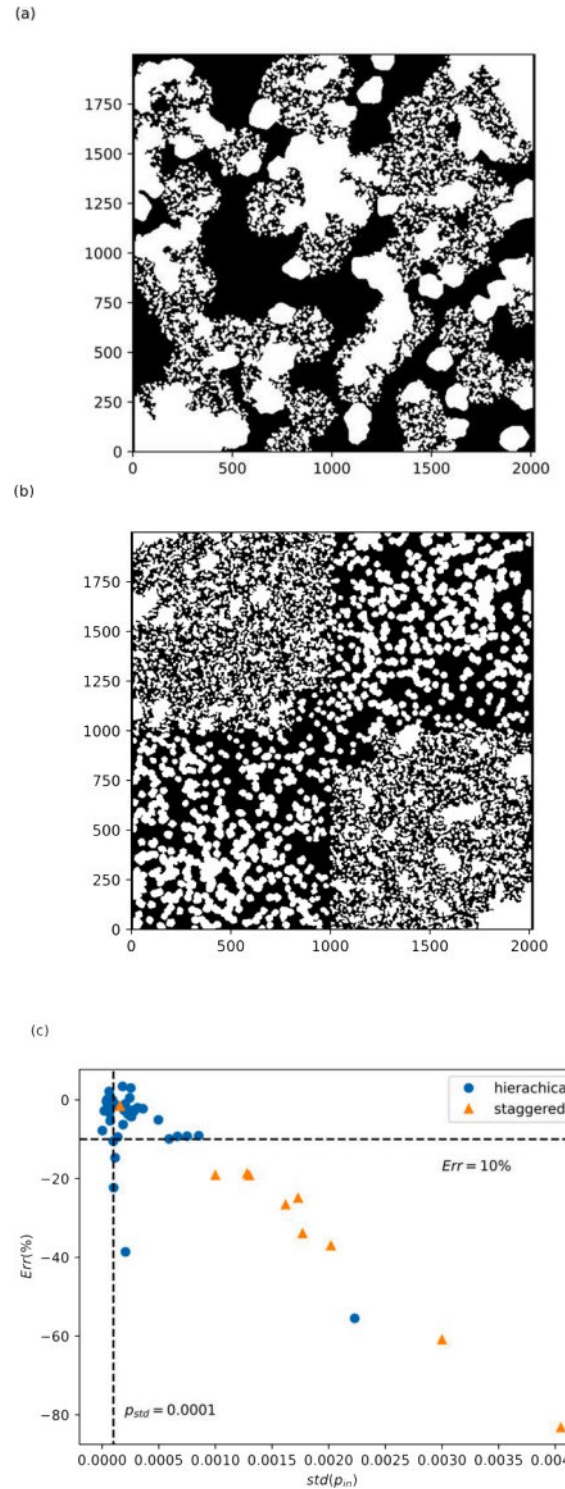


Fig. 13. (a, b) Illustration of the hierarchical porous media and the staggered porous media. The high permeability regions are staggered in staggered porous media. (c) The relative error as the function of the pressure standard deviation p_{std} at the inlet.

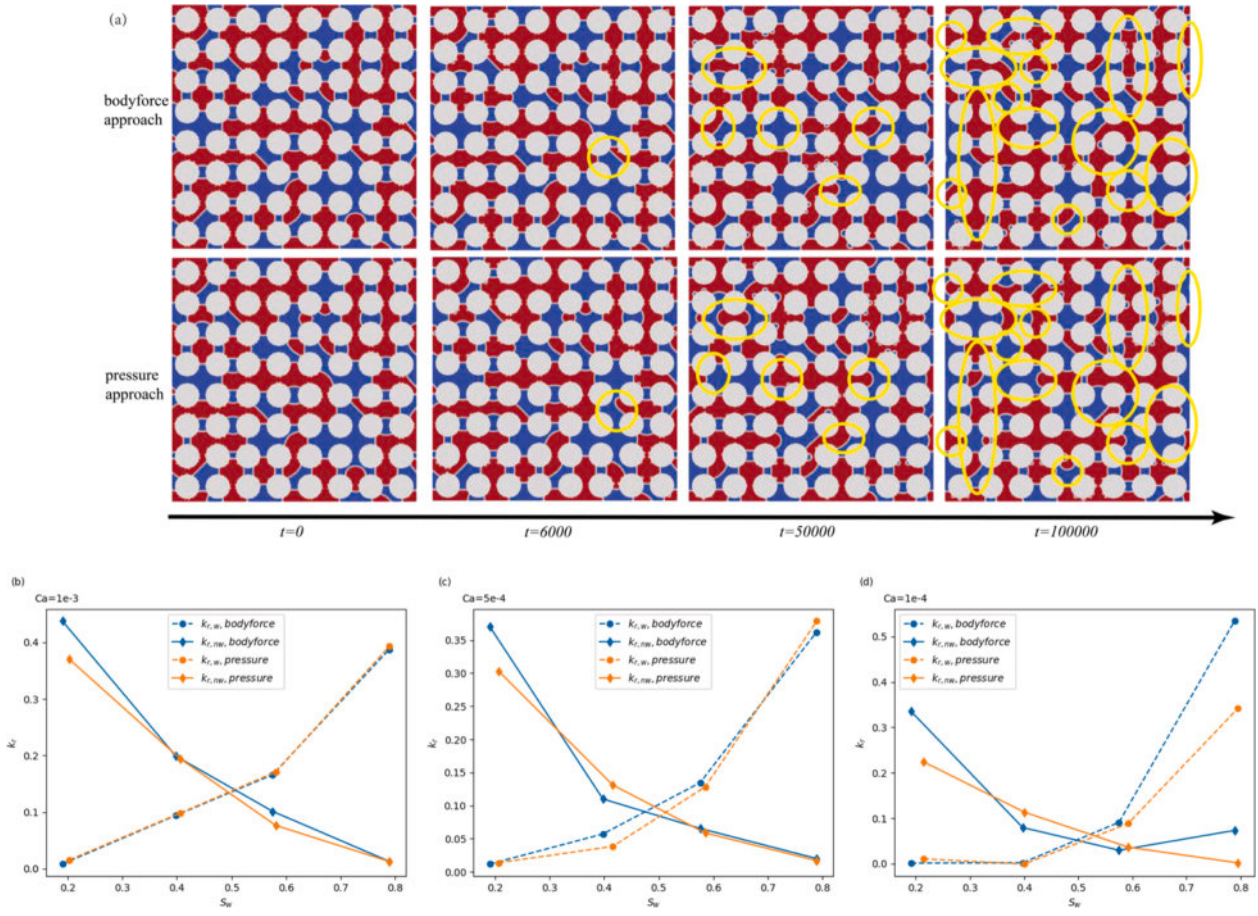


Fig. 14. (a) Evolution of the phase distribution on the regular structure over time. The blue phase is the wetting phase with a saturation of 40% and the contact angle is 75° $Ca = 5e - 4$. Top: body force approach; bottom: pressure approach. Some of the phase distribution differences are highlighted with yellow circles. From left to right: $t = 0$, $t = 6000$, $t = 50,000$ and $t = 100,000$. (b, c, d) The calculated relative permeability of the regular structure. The blue lines (dashed included) represent the body force approach while the orange lines (dashed included) represent the pressure approach. (b)-(d): $Ca = 1e - 3$, $Ca = 5e - 4$, and $Ca = 1e - 4$.

$$f_{i,0} = f_i^{eq} \left(\frac{3p_{in}}{c^2}, u_N \right) + f_{i,N}^{neq} = f_i^{++r} + f_{i,N}^{++b} - f_i^{eq}(\rho_N, u_N) + f_i^{eq} \left(\frac{3p_{in}}{c^2}, u_N \right),$$

$$f_{i,0}^b = \frac{f_{i,0}(1 - \phi_N)}{2}, \quad f_{i,0}^r = \frac{f_{i,0}(1 + \phi_N)}{2}, \tag{22}$$

where subscript 0 denotes the ghost node at inlet and N denotes the outlet node; $\phi_N = (\sum f_i^{++r} - \sum f_i^{++b})/\rho$ is the order parameter at outlet. The outlet boundary is vice versa.

3. Benchmark

3.1. Single-phase cases

To validate our models and code implementation, several benchmarks are conducted for both the single-phase and the multiphase flows. In this subsection, we present the benchmarks for the single-phase flow and multiphase flow in the subsequent subsection.

For single-phase flow, we select flow through the body-centered cubic (BCC) and face-centered cubic (FCC) structures, as shown in Fig. 1. shows. Regarding the periodic nature of BCC and FCC structures, the periodic boundary is applied at the cubic surface except the inlet and outlet. At the inlet and outlet, the pressure boundary is employed to maintain a constant pressure difference. The kinetic viscosity is 0.5, and the density is 1. The pressure difference Δp is 0.001 and lattice speed $c = 1$ for all cases. Consequently, the inlet pressure $p_{in} = 0.334$ and the outlet pressure $p_{out} = 0.333$. The permeability can be calculated via the

Darcy's law, i.e.

$$\frac{Q}{L^2} = \frac{k \Delta p}{\nu L}, \tag{23}$$

where L is the structure size and Q denotes the flow rate measured in simulations. The simulation results are shown and compared with the theoretical results in Table 1. The relative error is smaller than 3% for both structures which indicates that our single-phase flow solver can correctly predict the permeability of porous media.

3.2. Multiphase flows

The CG-CSF model employed in this work has undergone extensive benchmarking in literatures [5,62]. Common benchmarks, such as the stationary bubble test and the droplet attached to the wall test which validate the interfacial tension and the contact angle, can be found in our previous work [72]. In this work, the primary focus is on benchmarking the new periodic-pressure boundary. For this purpose, the layered flow [60] is selected as the benchmark case where the phase interface consistently intersects with the inlet and outlet boundaries. Previously, due to the numerical instability of the pressure boundaries, this benchmark was only conducted via the body force and periodic boundaries [11,41,73,74]. To the best of our knowledge, we are the first to perform this benchmark in pressure boundaries.

As illustrated in Fig. 2., the two phases flow concurrently between the two parallel plates driven by either the body force or the pressure gradient. The non-wetting phase flows between the wetting phase and

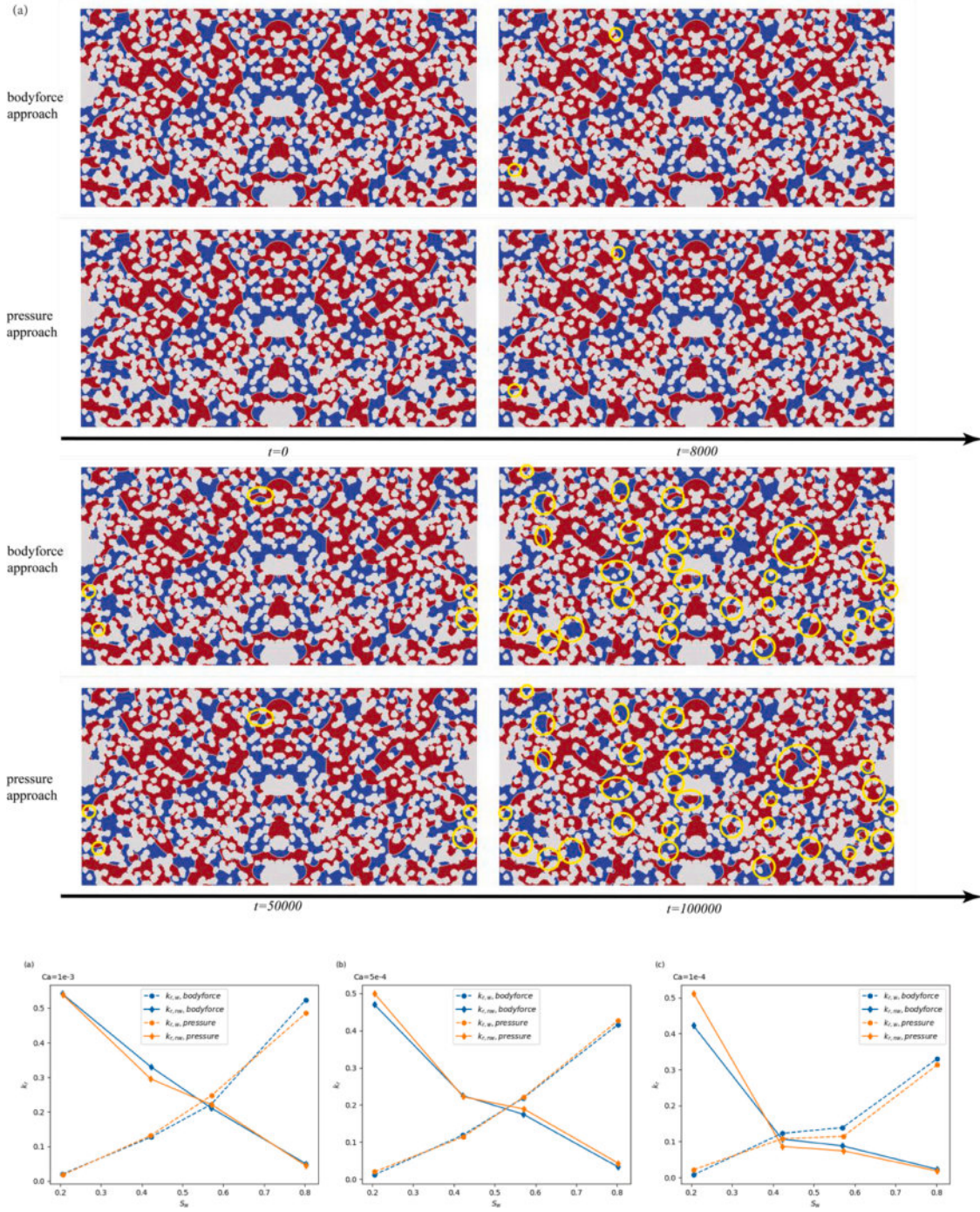


Fig. 15. (a) Evolution of the phase distribution on the randomly generated structure over time. The blue phase is the wetting phase with a saturation of 40% and the contact angle is 75° $Ca = 5e - 4$. Some of the phase distribution differences are highlighted with yellow circles. Top: body force approach; bottom: pressure approach. From top to bottom, left to right: $t = 0$, $t = 8000$, $t = 50,000$ and $t = 100,000$. (b, c, d) The calculated relative permeability of the randomly generated structure. The blue lines (dashed included) represent the body force approach while the orange lines (dashed included) represent the pressure approach. (b)-(d): $Ca = 1e - 3$, $Ca = 5e - 4$, and $Ca = 1e - 4$.

does not contact the wall, forming a layered structure. The analytical solution of such flow is given [74],

$$u(y) = \begin{cases} -\frac{F}{2\rho_b\nu_b}y^2 + \frac{fH}{2\rho_b\nu_b}y, & 0 \leq y < \frac{H-h}{2} \text{ or } \frac{H+h}{2} < y \leq H, \\ -\frac{F}{2\rho_r\nu_r}y^2 + \frac{FH}{2\rho_r\nu_r}y + \frac{F}{2\rho_b\nu_b} \frac{H^2-h^2}{4}, & \frac{H-h}{2} \leq y \leq \frac{H+h}{2}, \end{cases} \quad (24)$$

where H denotes the channel width and h is width of the non-wetting

phase layer; F represents the external body force or pressure gradient. In this benchmark, we set $\sigma = 0.06$, $L = 51$, $H = 100$ and $h = 50$. The viscosity ratio $M = \frac{\rho_r\nu_r}{\rho_b\nu_b}$ is set as 0.1 and 10. The inlet pressure $p_{in} = 0.33335$ and the outlet pressure $p_{out} = 0.33333$ for the pressure boundary case. The equivalent body force $F = 3.92 \times 10^{-7}$. The simulated results are presented in Fig. 2(b, c), which demonstrates a good agreement with the analytical solution for both body force and pressure boundary.

We also present the validation of the mass conservation as shown in

Fig. 3. The current pressure boundary slightly violates the conservation of mass, causing a slow increase in the saturation of the red phase over time (note that the variation of the saturation is smaller than 10^{-4}). However, as the lattice speed c increases, this non-conservation is reduced significantly. This is because the density difference between the inlet and outlet $\Delta\rho = 3c^2\Delta p$ is proportional to the pressure difference Δp and the square of the lattice speed c . When $\Delta\rho = \Delta p = 0$, the current boundary can completely degrade into a periodic boundary that conserves mass. Therefore, a large lattice speed c is adopted for all the subsequent multiphase-flow simulations, to maintain negligible mass and saturation variations.

4. Result and discussion

4.1. Numerical setup

The numerical setup follows the common approach used in the permeability and relative permeability calculations [27,30]. In the permeability calculation, a buffer region is padded at the inlet and outlet to create a periodic flow-path for random porous media as shown in Fig. 4. The boundary condition is either the pressure boundary introduced in Section 2.1, or a periodic boundary with an equivalent body force. No-slip wall is applied to other boundaries.

To calculate the relative permeability calculation, as illustrated in Fig. 4(b), we begin by generating a block-wise random phase distribution with a predetermined saturation in the pore space. To ensure a periodic flow-path and constant saturation in the system, both the phase distribution and the structure are flipped [30,41]. Subsequently, we conduct a multiphase simulation using periodic boundary conditions without body force, which allows us to achieve a phase distribution that is locally thermal equilibrium as Fig. 4(c). Finally, the resulting phase distribution is used as the initial condition for comparing the body force and pressure boundary. The body force with the periodic boundary equals to the pressure gradient in the pressure boundary.

4.2. Homogeneous structures

Firstly, we present the simulation results on the Darcy scale homogeneous structures. The sandstone-like porous media are generated by QSGS method [75], which provides a better representation of natural homogeneous random porous media. An example of generated structure is presented in Fig. 4. Although from the microscopic point of view, such structures are heterogeneous, however, they are considered homogeneous at Darcy scale (hereafter). It should also be noted that the homogeneous structures in this work correspond to the disordered heterogeneous porous structures in [31] as the seeds in this work are randomly generated. The structure sizes are 2000×2000 with a mean pore size around 24 pixels. The porosities are 55%.

As is shown in Table 2, the differences between the pressure approach and body force model are lower than 7% (absolute value, hereafter) for all structures we considered. Most results (8/10) are lower than 4%, which is acceptable for the permeability calculations. This can be attributed to the fact that the constant body force in body force approach, being a conservative force, can be interpreted as the gradient of a certain potential. In other words, for the Navier-Stokes equation,

$$\rho \left(\frac{\partial u}{\partial t} + u \cdot \nabla u \right) = -\nabla p + F_x + \mu \Delta u = -\nabla(p - f_x x) + \mu \Delta u \quad (25)$$

where $F = -\nabla(f_x x)$ the one-dimensional constant body force in the body force model. Define the effective pressure $\psi = p - f_x x$, Eq. (25) is identical to the Navier-Stokes equation without any external body force. Theoretically, the solution to Eq. (25) is identical provided that the boundary conditions are also identical. This suggests that though the constant body force initiates a uniform pressure gradient in the computational domain, the real pressure field will compensate

adaptively according to the flow field.

To further demonstrate this idea, we present the simulated pressure field and the velocity field of the two approaches as Fig. 5 shows. For the body force approach, we present the effective pressure $\psi = p - f_x x$ which should be equivalent to the pressure field in the pressure approach. According to Fig. 5, although some small quantitative differences can be observed in certain regions, the overall qualitative agreement between the pressure and velocity fields obtained from the two approach is consistent. Such small differences could be due to the compressibility error and flow heterogeneity. It can be observed that for the body force approach, the effective pressure at the inlet is not uniform due to the flow heterogeneity, while for the pressure boundary, the inlet pressure is fixed. Additionally, the velocity field is slightly different in the boundary region due to the periodic boundary in the body force approach. However, since the structural and flow heterogeneity is modest for homogeneous structures in this section, the boundary effect can be safely ignored in the permeability calculation.

The aforementioned analysis on N-S equation is not limited to small Re . Therefore, the results of different Re are presented in Table 3. The relative error is smaller than 4% for Re ranging from 0.001 to 10 as predicted. Similar results on pressure field and velocity field can be observed for larger Re as Fig. 6 shows.

4.3. Effect of the preferential path

According to the section above, it can be observed that one major error between the body force approach and pressure approach is the boundary effect induced by periodic boundary condition in the body force approach. For strong heterogeneous porous media, such difference will more significant.

Consider a ‘‘fracture-matrix’’ porous medium with a straight inclined fracture as Fig. 7 shows. Due to the permeability difference, the fracture naturally forms the preferential path. Such preferential path is a simplified representation of the random preferential paths due to structural heterogeneity, fractures and other factors. The porous medium has a length of L and a buffer region with width h . In addition, there is a preferential path that is inclined at an angle of θ with the width D and length l . The permeability along the preferential path is typically of greater interest, so we assume that $\theta < 45^\circ$.

Through Π theorem, 4 non-dimensional number can be found, i.e., θ , h/D , L/D and Re . The preferential path width $D = 30$ is selected as the characteristic size. Firstly, we assume the matrix region is impermeable. At low Re , the flows in the preferential path and the buffer region follow the Poiseuille equation, respectively. In the preferential path region, the mean velocity u_m can be expressed as,

$$u_m = \frac{D^2 f L}{12 \mu l} = \frac{D^2 f}{12 \mu} \cos(\theta) \quad (26)$$

The mean velocity in the buffer region u'_m can be calculated via,

$$u'_m = \frac{u_m D}{h} \quad (27)$$

Thus, the resistance of the buffer region R is

$$R = \frac{12 u'_m \mu L \tan(\theta)}{h^2} = \left(\frac{D}{h} \right)^3 \sin(\theta) f L \quad (28)$$

Let $\phi = f L / R$, the relative error is

$$Err = \frac{R}{R + f L} = \frac{1}{1 + \phi} \quad (29)$$

$$\phi = \frac{f L}{R} = \left(\frac{h}{D} \right)^3 \frac{1}{\sin(\theta)} \quad (30)$$

The physical meaning of ϕ is the resistance of the porous media over that of the buffer region. The relative error approaches 0 if the resistance

of the porous media is much more significant than that of the buffer region, i.e., ϕ approaches infinity.

A direct finding of Eqs. (29), (30) is that the relative error is irrelevant to the length of the porous media. This is confirmed by the simulation data presented in Fig. 8(a), where we can see that when $L > 600$, the length of the porous media has a negligible effect on ϕ and the relative error. The deviation from the theoretical prediction could be attributed to the corners of flow channel. Thus, the length of the porous media is fixed to be 600 for all subsequent simulations. The effect of the buffer size h and the inclined-angle θ is illustrated in Fig. 8(b, c). It can be observed that Eq. (25) agrees well with the simulation results. Fig. 9 shows a comparison between the relative error calculated using Eq. (29) and our simulation results. We find good agreement for low and middle Re . However, at high $Re \approx 12$, some errors are observed due to the inertial effect. Nonetheless, we still achieve qualitative agreement regarding the buffer size effect.

Eqs. (25)–(30) provide an intuitive explanation on the computational error induced by body force approach. Due to the periodic boundary in the body force approach, the flow resistance across the boundary, i.e., the flow resistance in the buffer region is not negligible for strong preferential flow, resulting underestimation of the permeability. The relative errors can reach as high as 80% for theoretical “z-shape” structures. Thus, the relative errors can be reduced via reducing the flow resistance in the buffer regions, in other words, adopting larger buffer regions. According to Eqs. (29), (30), the relative errors will decrease rapidly as the buffer size h increases.

Then we further consider the real fracture-matrix porous media with a permeable matrix. Fig. 10 shows the calculated permeability of a generated fracture-matrix structure via the body force approach and the pressure approach. The impact of the buffer size on the calculated permeability via the body force approach is much more significant than that with the pressure approach. For small buffer sizes, the permeability is underestimated in the body force approach due to the periodic boundary. The pressure field and the velocity field are displayed in Fig. 11. In the body force approach, the presence of a strong vertical flow in the buffer region results in an overall increase in the resistance of the structure, which reduces the total flux. Additionally, the (effective) pressure field experiences greater non-uniformity at the boundary, which is responsible for driving the vertical flow. Therefore, the pressure difference can be employed to evaluate the error induced by the body force approach. On the one hand, the pressure non-uniformity at boundary is the result of the periodic boundary coupled with the structural heterogeneity. On the other hand, for Eq. (25), the boundary non-uniformity pressure is distinct from the pressure boundary, resulting different solutions.

Fig. 12 shows the relative error in the pressure non-uniformity at boundary, which is measured by the pressure standard deviation p_{std} at the inlet for different inclined angles, buffer sizes as well as two mean matrix pore sizes. To reduce the random error of randomly generated structures, 5 structures are generated for each set of parameters, resulting in a total of over 300 structures. The results demonstrate that the error of the body force approach increases consistently with increasing pressure standard deviation, indicating that the pressure standard deviation can be employed as the heterogeneity parameter. The physical meaning of this heterogeneity parameter describes the heterogeneity of the pressure under periodic boundaries. $p_{std} < 0.0001$ is suggested to achieve $Err < 10\%$.

Two more typical structures with preferential paths are examined as well, as Fig. 13 shows. Due to the differences in structural heterogeneity, the results are more discrete. However, the criterion of $p_{std} < 0.0001$ still roughly valid.

4.4. Effect of multiphase flow

In this section, we first present the results of the regular structure. Since the regular structure is already periodic, the flipping step in the

numerical setup is omitted. The structure is 400×400 with 64 cell units. The capillary number $Ca = Q\nu/A\sigma$, where Q is the total flow rate and A , ν denote cross-section area and kinetic viscosity. The surface tension $\sigma = 0.06$ and viscosity ν is 0.5 for all cases and fluid phases. The body force or pressure difference is adjusted adaptively to keep the prescribed Ca .

As Fig. 14 shows, initially the phase distributions for both approaches are the same. However, at the early stage of simulations ($t = 6000$), we observe some differences in the phase distributions. In the previous studies and this work, minor errors are observed in velocity field for body force approaches [20,21,46]. Such differences will be amplified due to strong coupling of the transportation of menisci and local velocity field. As time progresses, the differences in the phase distributions of the two approaches increase. Therefore, it is inappropriate to simulate pressure boundary via body force for multiphase flows.

To provide a quantitatively comparison, we calculate the relative permeability of the structure. The relative permeability is defined via the two-phase Darcy's equation. At the given saturation of the wetting fluid S_w ,

$$k_{r,w} = \frac{Q_w(S_w)F}{QF(S_w)}, \quad k_{r,nw}(S_w) = \frac{Q_{nw}(S_w)F}{QF(S_w)}, \quad (31)$$

where k_r represents the relative permeability and w, nw represent wetting and non-wetting phase, respectively. As mentioned above, the total flow rate $Q = Q_w + Q_{nw}$ is kept constant for all saturations, while the body force or pressure gradient is monitored directly from the simulation results. The relative permeability is calculated till the body force or pressure difference reaches the steady state approximately.

From a statistical point of view, the differences of the relative permeability are only significant at low Ca , as demonstrated in Fig. 14 (b, c, d). This can be explained by the definition of Ca . The interfacial tension plays a more important role at low Ca . For higher Ca , although the phase distributions evolve differently in two approaches, the relative permeability is dominated by the driven force rather than internal interfacial tension, resulting smaller errors.

While for randomly generated structures, the qualitatively law is the same while, surprisingly, the quantitatively errors are much smaller compared to regular structures as demonstrated in Fig. 15. The randomly generated structure is 800×800 with a mean pore size of 12. Typically, it is expected that for regular, uniform structures, the errors will be smaller as in the case of single-phase flows. For regular structures, the pore sizes are the same, resulting identical characteristic capillary pressures. Therefore, there could be multiple menisci having identical mobilization capillary pressures at the same time. Nevertheless, the mobilization capillary pressure is ordered in random structures due to the distribution of the pore sizes. In other words, random structures exhibit a stronger structural effect in multiphase flows. Therefore, fewer differences in the phase distribution are observed in random structures as Fig. 15(a) shows.

5. Conclusion

This study examines the suitability of using the body force model to simulate the pressure boundary for porous flows. The absolute permeability and the relative permeability are selected as benchmark cases to quantify the errors induced by the body force model. For single-phase flows, a comprehensive analysis is conducted via the Navier-Stokes equation. For homogeneous structures, the errors of the body force model are within 5% for most cases. However, for structures with the preferential paths, due to the periodic boundary in the body force approach, the relative errors can be as high as 80%. A new heterogeneity parameter, the boundary pressure non-uniformity which is quantified via the standard deviation, is proposed. We suggest $p_{std} < 0.0001$ for permeability calculations. The periodic pressure boundary by Kim and

Pitsch [21] is extended to color-gradient LBM. With the large lattice speed c , we obtain acceptable mass conservation results. For the multiphase flows, the differences in phase distributions between the body force approach and the pressure approach appear at the early stage of the simulations, which is irreversible. Therefore, the relative permeability difference is significant at low Ca where the interfacial tension, i. e., the phase distribution dominates the flows. For larger Ca , this error is less significant statistically. Although only fluid flow is considered in this work, it should be pointed out that other transport processes including heat and mass transfers, electro-kinetic flows could also be influenced by the flow field. Consequently, it is important to consider the structural heterogeneity and proper parameters when employing body force model.

Declaration of Competing Interest

The authors declare that they have no known competing financial interests or personal relationships that could have appeared to influence the work reported in this paper.

Data availability

No data was used for the research described in the article.

Acknowledgments

This work is financially supported by the National Key R&D Program of China [2019YFA0708704] and the NSF grant of China [12272207].

References

- Thomas S. Enhanced oil recovery - an overview. *Oil Gas Sci. Technol.* 2007;63(1): 9. - *Revue de l'IFP*.
- Bear J, Cheng AHD. *Modeling groundwater flow and contaminant transport*. Dordrecht: Springer; 2010.
- Brandon NP, Brett DJ. Engineering porous materials for fuel cell applications. *Philos Trans A Math Phys Eng Sci* 2006;364(1838):147.
- Abidoye LK, Khudaïda KJ, Das DB. Geological carbon sequestration in the context of two-phase flow in porous media: a review. *Crit Rev Environ Sci Technol* 2014;45(11):1105.
- Chen Y, et al. Inertial effects during the process of supercritical CO₂ Displacing brine in a sandstone: lattice Boltzmann simulations based on the continuum-surface-force and geometrical wetting models. *Water Resour Res* 2019;55(12): 11144.
- Tölke J, Krafczyk M. TeraFLOP computing on a desktop PC with GPUs for 3D CFD. *Int J Comput Fluid Dyn* 2008;22(7):443.
- Herschlag G, et al. Analysis of GPU data access patterns on complex geometries for the D3Q19 Lattice Boltzmann algorithm. *IEEE Trans Parallel Distrib Syst* 2021;32(10):2400.
- Zheng J, et al. Characterization of spontaneous imbibition dynamics in irregular channels by mesoscopic modeling. *Comput Fluids* 2018;168:21.
- Xie C, et al. Self-adaptive preferential flow control using displacing fluid with dispersed polymers in heterogeneous porous media. *J Fluid Mech* 2020;906:A10.
- Liu T, Jin X, Wang M. Critical resolution and sample size of digital rock analysis for unconventional reservoirs. *Energies* 2018;11(7):111.
- Xie C, et al. An improved pore-network model including viscous coupling effects using direct simulation by the lattice Boltzmann method. *Adv Water Res* 2017;100: 26.
- Xie C, Lei W, Wang M. Lattice Boltzmann model for three-phase viscoelastic fluid flow. *Phys Rev E* 2018;97(2-1):023312.
- Ren X, et al. Optimization and Implementation of LBM Benchmark on Multithreaded GPU. In: *Proceedings of the 2010 international conference on data storage and data engineering*; 2010. p. 116.
- Buckles J, et al. Flow through porous media using lattice Boltzmann method. *Los Alamos Sci* 1994;22:112.
- Chen S, Doolen GD. Lattice Boltzmann method for fluid flows. *Annu Rev Fluid Mech* 1998;30:329.
- Ferreol, B. and D.H. Rothman, Lattice-Boltzmann simulations of flow through Fontainebleau sandstone. *Multiphase flow in porous media*, 1995: p. 3.
- Zou Q, He X. On pressure and velocity boundary conditions for the lattice Boltzmann BGK model. *Phys Fluids* 1997;9(6):1591.
- Guo Z, Zheng C, Shi B. Non-equilibrium extrapolation method for velocity and pressure boundary conditions in the lattice Boltzmann method. *Chin Phys* 2002;11(4):366.
- Ginzburg I, Verhaeghe F, d'Humieres D. Two-relaxation-time lattice Boltzmann scheme: about parametrization, velocity, pressure and mixed boundary conditions. *Commun Comput Phys* 2008;3(2):427.
- Zhang J, Kwok DY. Pressure boundary condition of the lattice Boltzmann method for fully developed periodic flows. *Phys Rev E Stat Nonlinear Soft Matter Phys* 2006;73(4 Pt 2):047702.
- Kim SH, Pitsch H. A generalized periodic boundary condition for lattice Boltzmann method simulation of a pressure driven flow in a periodic geometry. *Phys Fluids* 2007;19(10):108101.
- Shan, X. and H. Chen, Lattice Boltzmann model for simulating flows with multiple phases and components. *Phys. Rev. E Stat. Phys. Plasmas Fluids Relat. Interdiscip. Topics*, 1993. 47(3): p. 1815.
- Huang J, Xiao F, Yin X. Lattice Boltzmann simulation of pressure-driven two-phase flows in capillary tube and porous medium. *Comput Fluids* 2017;155:134.
- Leclaire S, et al. Multiphase periodic pressure difference boundary condition enhanced by a proportional-integral-derivative controller for the lattice Boltzmann method. *Int J Numer Methods Fluids* 2018;88(9):434.
- Wang Z, et al. Two pressure boundary conditions for multi-component multiphase flow simulations using the pseudo-potential lattice Boltzmann model. *Comput Fluids* 2022;248:105672.
- Lou Q, Guo Z, Shi B. Evaluation of outflow boundary conditions for two-phase lattice Boltzmann equation. *Phys Rev E Stat Nonlinear Soft Matter Phys* 2013;87(6):066301.
- Li H, Pan C, Miller CT. Pore-scale investigation of viscous coupling effects for two-phase flow in porous media. *Phys Rev E Stat Nonlinear Soft Matter Phys* 2005;72(2 Pt 2):026705.
- Buckles JJ, et al. Toward improved prediction of reservoir flow performance. *Los Alamos Sci* 1994;22:112.
- Ferreol B, Rothman DH. Lattice-Boltzmann simulations of flow through Fontainebleau sandstone. *Multiphase flow in porous media*. Springer; 1995. p. 3.
- Jiang F, Tsuji T. Changes in pore geometry and relative permeability caused by carbonate precipitation in porous media. *Phys Rev E Stat Nonlinear Soft Matter Phys* 2014;90(5-1):053306.
- Zakirov TR, Khramchenkov MG. Study of the pore space heterogeneity effect on the absolute permeability tensors calculated under different boundary conditions and driving forces using a "Computational Rock Physics" technology. *J Pet Sci Eng* 2022;216:110750.
- Jiang F, Tsuji T. Estimation of three-phase relative permeability by simulating fluid dynamics directly on rock-microstructure images. *Water Resour Res* 2017;53(1): 11.
- Pico CE, dos Santos LO, Philippi PC. lattice-Boltzmann simulation of two-phase fluid flow through porous media. In: *Proceedings of the 18th international congress of mechanical engineering*. Citeseer; 2005.
- Hao L, Cheng P. Pore-scale simulations on relative permeabilities of porous media by lattice Boltzmann method. *Int J Heat Mass Transf* 2010;53(9-10):1908.
- Ramstad T, et al. Relative permeability calculations from two-phase flow simulations directly on digital images of porous rocks. *Transp Porous Media* 2011; 94(2):487.
- Liu H, et al. Multiphase lattice Boltzmann simulations for porous media applications. *Comput Geosci* 2015;20(4):777.
- Suwandi N, Jiang F, Tsuji T. Relative permeability variation depending on viscosity ratio and capillary number. *Water Resour Res* 2022;58(6):62933.
- Boek ES, et al. Multiphase-flow and reactive-transport validation studies at the pore scale by use of lattice boltzmann computer simulations. *SPE J* 2017;22(03): 940.
- Alpak FO, Berg S, Zacharoudiou I. Prediction of fluid topology and relative permeability in imbibition in sandstone rock by direct numerical simulation. *Adv Water Res* 2018;122:49.
- Shi Y, Tang GH. Relative permeability of two-phase flow in three-dimensional porous media using the lattice Boltzmann method. *Int J Heat Fluid Flow* 2018;73: 101.
- Liu T, Wang M. Critical REV size of multiphase flow in porous media for upscaling by pore-scale modeling. *Transp Porous Media* 2022;144:111.
- Wang M, et al. Electrokinetic pumping effects of charged porous media in microchannels using the lattice Poisson-Boltzmann method. *J Colloid Interface Sci* 2006;304(1):246.
- Wang M, et al. Lattice Poisson-Boltzmann simulations of electroosmotic flows in charged anisotropic porous media. *Commun Comput Phys* 2007;2(6):1055.
- Hlushkou D, et al. Pore-scale dispersion in electrokinetic flow through a random sphere packing. *Anal Chem* 2007;79(1):113.
- Alpak FO, et al. Direct simulation of pore-scale two-phase visco-capillary flow on large digital rock images using a phase-field lattice Boltzmann method on general-purpose graphics processing units. *Comput Geosci* 2019;23(5):849.
- Kandhai D, et al. Implementation aspects of 3D lattice-BGK: boundaries, accuracy, and a new fast relaxation method. *J Comput Phys* 1999;150(2):482.
- Rustamov N, Douglas CC, Aryana SA. Scalable simulation of pressure gradient-driven transport of rarefied gases in complex permeable media using Lattice Boltzmann Method. *Fluids* 2022;8(1):1.
- Qian YH, d'Humières D, Lallemand P. Lattice BGK models for Navier-Stokes equation. *EPL (Europhysics Letters)* 1992;17(6):479.
- Krüger T, et al. *The lattice Boltzmann method: principles and practice*. Switzerland: Springer; 2017.
- Guo Z, Zheng C, Shi B. Discrete lattice effects on the forcing term in the lattice Boltzmann method. *Phys Rev E Stat Nonlinear Soft Matter Phys* 2002;65(4 Pt 2B): 046308.

- [51] Luo LS, et al. Numerics of the lattice Boltzmann method: effects of collision models on the lattice Boltzmann simulations. *Phys Rev E Stat Nonlinear Soft Matter Phys* 2011;83(5 Pt 2):056710.
- [52] d'Humieres D, et al. Multiple-relaxation-time lattice Boltzmann models in three dimensions. *Philos Trans A Math Phys Eng Sci* 2002;360(1792):437.
- [53] d'Humieres D. Generalized lattice Boltzmann equations. *Rarefied gas dynamics: theory and simulations*, 159. Washington, DC: AIAA; 1992. p. 450. *Prog. Astronaut. Aeronaut. edited by B. D. Shizgal and D. P. Weave.*
- [54] Guo Z, Zheng C. Analysis of lattice Boltzmann equation for microscale gas flows: relaxation times, boundary conditions and the Knudsen layer. *Int J Comput Fluid Dyn* 2008;22(7):465.
- [55] Chai Z, Zhao TS. Effect of the forcing term in the multiple-relaxation-time lattice Boltzmann equation on the shear stress or the strain rate tensor. *Phys Rev E Stat Nonlinear Soft Matter Phys* 2012;86(1 Pt 2):016705.
- [56] Guo Z, Shu C. *Lattice Boltzmann method and its application in engineering*, 3. Singapore: World Scientific; 2013.
- [57] Lallemand, P. and L.S. Luo, Theory of the lattice Boltzmann method: dispersion, dissipation, isotropy, galilean invariance, and stability. *Phys Rev E Stat Phys Plasmas Fluids Relat. Interdiscip. Topics*, 2000. 61(6 Pt A): p. 6546.
- [58] Rothman DH, Keller JM. Immiscible cellular-automaton fluids. *J Stat Phys* 1988;52(3–4):1119.
- [59] Gunstensen AK, et al. Lattice Boltzmann model of immiscible fluids. *Phys Rev A* 1991;43(8):4320.
- [60] Huang H, Sukop M, Lu X. *Multiphase lattice Boltzmann methods: theory and application*. West Sussex: Wiley; 2015.
- [61] Liu H, Valocchi AJ, Kang Q. Three-dimensional lattice Boltzmann model for immiscible two-phase flow simulations. *Phys Rev E Stat Nonlinear Soft Matter Phys* 2012;85(4 Pt 2):046309.
- [62] Xu Z, Liu H, Valocchi AJ. Lattice Boltzmann simulation of immiscible two-phase flow with capillary valve effect in porous media. *Water Resour Res* 2017;53(5): 3770.
- [63] Latva-Kokko M, Rothman DH. Diffusion properties of gradient-based lattice Boltzmann models of immiscible fluids. *Phys Rev E Stat Nonlinear Soft Matter Phys* 2005;71(5 Pt 2):056702.
- [64] Leclaire S, et al. Generalized three-dimensional lattice Boltzmann color-gradient method for immiscible two-phase pore-scale imbibition and drainage in porous media. *Phys Rev E* 2017;95(3–1):033306.
- [65] Leclaire S, Reggio M, Trépanier JY. Isotropic color gradient for simulating very high-density ratios with a two-phase flow lattice Boltzmann model. *Comput Fluids* 2011;48(1):98.
- [66] Grunau D, Chen S, Eggert K. A lattice Boltzmann model for multiphase fluid flows. *Phys Fluids A* 1993;5(10):2557.
- [67] Akai T, Bijeljic B, Blunt MJ. Wetting boundary condition for the color-gradient lattice Boltzmann method: validation with analytical and experimental data. *Adv Water Resour* 2018;116:56.
- [68] Sbragaglia M, et al. Generalized lattice Boltzmann method with multirange pseudopotential. *Phys Rev E Stat Nonlinear Soft Matter Phys* 2007;75(2 Pt 2): 026702.
- [69] Yu Y, et al. Color-gradient lattice Boltzmann modeling of immiscible two-phase flows on partially wetting surfaces. *Proc Inst Mech Eng Part C J Mech Eng Sci* 2017; 232(3):416.
- [70] Graser O, Grimm A. Adaptive generalized periodic boundary conditions for lattice Boltzmann simulations of pressure-driven flows through confined repetitive geometries. *Phys Rev E Stat Nonlinear Soft Matter Phys* 2010;82(1 Pt 2):016702.
- [71] Chapman A, Higdon JJ. Oscillatory Stokes flow in periodic porous media. *Phys Fluids A* 1992;4(10):2099.
- [72] Yang G, Wang M. Surface roughness effect on dynamic wettability in imbibition process. *Comput Fluids* 2023;263:105959.
- [73] Ba Y, et al. Multiple-relaxation-time color-gradient lattice Boltzmann model for simulating two-phase flows with high density ratio. *Phys Rev E* 2016;94(2–1): 023310.
- [74] Porter ML, et al. Multicomponent interparticle-potential lattice Boltzmann model for fluids with large viscosity ratios. *Phys Rev E Stat Nonlinear Soft Matter Phys* 2012;86(3 Pt 2):036701.
- [75] Wang M, et al. Mesoscopic predictions of the effective thermal conductivity for microscale random porous media. *Phys Rev E Stat Nonlinear Soft Matter Phys* 2007;75(3 Pt 2):036702.
- [76] Wang W, et al. *Experimental and numerical study of mixing behavior inside droplets in microchannels*. *AIChE Journal* 2013;59(5):1801–13.